Rock and Soil Mechanics

Volume 41 | Issue 8 Article 10

1-22-2021

Study on boundary effect of embedded optical fiber sensor in tunnel structure

Gong-yu HOU
School of Mining Engineering, Xinjiang Institute of Engineering, Urumchi, Xinjiang 830091, China

Zi-xiang LI
School of Mechanics and Civil Engineering, China University of Mining and Technology(Beijing), Beijing 100083, China, lzx4269016@163.com

Tao HU
School of Mechanics and Civil Engineering, China University of Mining and Technology(Beijing), Beijing 100083, China

Tian-ci ZHOU
School of Mechanics and Civil Engineering, China University of Mining and Technology(Beijing), Beijing 100083, China

See next page for additional authors

Custom Citation

HOU Gong-yu, LI Zi-xiang, HU Tao, ZHOU Tian-ci, XIAO Hai-lin, . Study on boundary effect of embedded optical fiber sensor in tunnel structure[J]. Rock and Soil Mechanics, 2020, 41(8): 2839-2856.

Study on boundary effect of embedded optical fiber sensor in tunnel structure

Authors
Gong-yu HOU, Zi-xiang LI, Tao HU, Tian-ci ZHOU, and Hai-lin XIAO

Rock and Soil Mechanics 2020 41(8): 2839–2850 ISSN 1000–7598
https: //doi.org/10.16285/j.rsm.2019.6834 rocksoilmech.researchcommons.org/journal

Study on boundary effect of embedded optical fiber sensor in tunnel structure

HOU Gong-yu[1, 2], LI Zi-xiang[1], HU Tao[1], ZHOU Tian-ci[1], XIAO Hai-lin[1]

1. School of Mechanics and Civil Engineering, China University of Mining and Technology(Beijing), Beijing 100083, China

2. School of Mining Engineering, Xinjiang Institute of Engineering, Urumchi, Xinjiang 830091, China

Abstract: To explore the boundary effect of the strain transmission between embedded optical fiber sensor and tunnel lining, the study was conducted from three aspects: theoretical, experimental studies and field applications. The results were verified in actual engineering. The strain transfer model of optical fiber in the concrete lining was constructed, and the mechanism of optical fiber strain transfer was analyzed. The strain transfer efficiency of optical fiber was then calculated and compared that with the numerical modeling results, which verified the accuracy of the mechanical calculation model. The concrete lining of tunnel was simulated with the reinforced concrete beams and distributed optical fibers were embedded on the surface of the concrete beams. Two groups of tests were carried out in this study. The test beams were loaded in stages and the optical fibers were tested by BOFDA technology. The test results show that the embedded fiber optic sensor has a boundary effect. The two ends of the beam structure are the low efficiency strain transmission area of the optical fibers, which cannot fully transfer the strain of the test beam. The middle part of the test beam is the high efficiency strain transfer area of the optical fibers, which can completely transfer the strain of the test beam. Based on the research results, the engineering application research was carried out. A distributed optical fiber sensor was installed in the tunnel lining in the CRD construction method section of the subway tunnel of the Beijing New Airport Line using the embedded fiber technology. The monitoring results show that the boundary effect has little influence on the monitoring results. The placement method of the distributed embedded optical fiber is feasible. This research can provide a reference for the application of distributed optical fiber technology in underground engineering structure monitoring.

Keywords: distributed optical fiber; coupling performance; tunnel monitoring; BOFDA technology

1 Introduction

In recent years, optical fiber sensing (network) monitoring technology has been widely used to monitor the structural health of geotechnical engineering projects such as Brillouin optical time domain reflection strain/temperature measurement technology (BOTDR), Brillouin optical time domain analysis strain/temperature measurement technology (BOTDA), Raman optical time domain reflection strain/temperature measurement technology (ROTDR) and Bragg grating measurement technology (FBG)[1–7]. In underground engineering monitoring projects, to ensure the optical fiber to deform together with the structure to be measured, the optical fiber usually requires to be combined with the structure under test in various ways. The inner optical fiber will be then deformed when the tested structure is deformed. The combined properties of the structure and the optical fiber determine whether the strain of the structure can be effectively transmitted to the optical fiber, as well as whether the monitoring data can reflect the true deformation of the structure. At present, scholars have studied the theory of strain transfer between optical fibers and structures to be measured. Tin was selected as the bonding material, Li et al.[8] proposed a strain transfer model for FBG and beams of equal strength using the surface bonding method. Shen et al.[9] studied the influence of the substrate material and size on strain transmission. Torres et al.[10] studied the effect of different adhesive thicknesses and different FBG packaging structures on strain transmission. Wang et al.[11] proposed a failure mechanism of the interface deboning of an embedded optical fiber sensor. Wu et al.[12] analyzed the influence of the FBG sensor length, the thickness of the bonding layer, and the elastic modulus on strain transmission. In the above mentioned researches, the boundary effect of strain transfer under the surface of an optical fiber was analyzed. As for the strain transfer model of the embedded optical fiber, many research works have been conducted by the research team of Nanjing University, China. Li et al.[13] designed a three-point bending test of the soil strip, and they found that the deformation coupling performance decreases as soil deformation increases gradually between the optical fiber and soil body. Yang et al.[14] studied the best mix ratio of grouting coupling material for the directly buried optical fiber sensing borehole. Cheng et al.[15] performed the coupling performance test of the fiber– soil interface, and they concluded that the interaction process of optical fiber–soil interface was divided into three stages: full coupling, semi-coupling, and relative sliding. Shi et al.[16] studied the evaluation of fiber– soil coupling in full section distributed optical fiber monitoring technology. Based on the classical strain transfer model and Goodman hypothesis, Zhang et al.[17] established a strain transfer model of the stratum– borehole backfills-

Received: 25 October 2019 Revised: 28 November 2019
This work was supported by the Central University Major Achievement Transformation Project in Beijing (ZDZH20141141301) and the National Natural Science Fund Committee and Shenhua Group Co., LTD. Jointly Funded Key Projects (U1261212，U1361210).
First author: HOU Gong-yu, male, born in 1965, PhD, Professor, PhD supervisor, research interests: rock mechanics, geotechnical engineering. E-mail: hgyht@126.com
Corresponding author: LI Zi-xiang, male, born in 1995, PhD candidate, majors in rock mechanics and tunnel health monitoring. E-mail: lzx4269016@163.com

sensing optical cable, and they studied the effects of sensing cable, backfill material, and stratum properties on the strain transfer characteristics. The researches provide a useful exploration for strain transfer theory of the embedded optical fiber sensor in the discrete objects such as rock and soil. In the structural monitoring using optical fiber, currently, most of the optical fibers are attached to the structure surface using an adhesive. Besides, the strain transfer of an optical fiber sensor has mostly been conducted based on the surface adhesion model. Although the strain transmission effect is relatively higher and the installation is relatively simple using the surface adhesion model, this method is not suitable for the complex monitoring environment of underground engineering. To improve the survival rate of optical fibers in such complex environments, it is often necessary to cover the optical fibers with a protective sleeve and insert the optical fiber into the testing structure and seal it for protection purposes. There is a lack of research on the strain transfer model for implanted distributed optical fibers in a structure. In addition to the theoretical research vacancies, the effect of the application of implanted optical fibers in practical engineering needs to be tested and the influence of boundary effect during the strain transmission on the monitoring result still needs to be studied.

Based on the distributed optical fiber sensing technology of Brillouin scattering and shear lag theory, in this study, a strain transfer model of distributed optical fibers embedded on a concrete structure surface is proposed. The accuracy of the model is verified by finite element analysis and laboratory testing. To verify the actual application of a practical engineering project, the distributed optical fiber monitoring technology was applied in the dismantling stage of tunnel temporary shoring through the distributed optical fiber monitoring project 07 in the Beijing Rail Transit New Airport Line. By embedding the optical fibers in the primary lining of the tunnel, the strain variation law of the tunnel was monitored in the process of demolishing the temporary support and the secondary lining stage. The feasibility of the implantation of the distributed optical fibers was systematically verified.

2 Theoretical analysis of the optical fiber strain transfer model

The main component of the bare optical fiber sensor is silicon dioxide for the optical fiber, which is a brittle material with poor shear resistance and easy to break. It is known that civil engineering construction is a typically extensive operation, in this consideration, the optical fibers have to be protected in practical application, no matter what type of layout method for the optical fibers. Due to the different stress transmission performances of the protective layers around the fiber, the strain of the structure will be different from the strain measured by the optical fiber sensor.

Optical fibers are embedded in slots on the surface of concrete structures. The slots are then backfilled and sealed with cement. At present, this is a common method of protecting optical fibers in engineering projects, as shown in Fig.1.

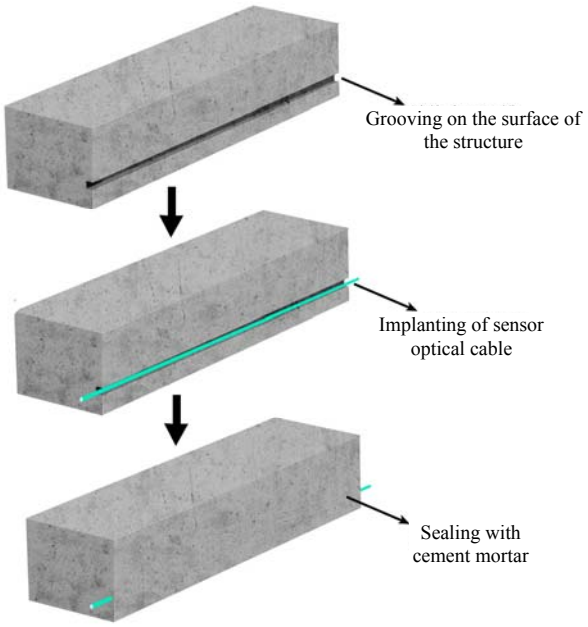

Fig. 1 Schematic diagram of embedded optical cable on slotted structural surface

The model in this section was mainly to study the strain transfer mechanism of optical fibers in this fiber protection condition. To facilitate the establishment of the model, it is necessary to make some reasonable assumptions according to the actual situation.

2.1 Assumptions

(1) The material has linear elastic properties, and the tested structure is subject to uniform strain along the axis of the optical fiber.

(2) The coating layer and the optical fiber core are regarded as a single structure, which is called the optical fiber layer. It should be mentioned that all the optical fibers that are used for sensing and monitoring are tightly wrapped cables. That is to say, the coating layer is firmly attached to the fiber core, and it is difficult to mechanically separate them. Therefore, no matter the packaging type, if the internal structure of the sensing cable slips, it will behave like the protective sleeve and the coating layer have separated, but the coating layer and the fiber core can still be tightly combined, as shown in Fig.2. Therefore, the coating layer and the fiber core can be considered as a single structure.

(3) The interface between the optical fiber and the protective sheath, as well as the protective sleeve and the structure is tightly attached and cannot fall off. It is considered that the strain difference between the optical fiber and the tested structure is mainly caused by the lag phenomenon of the shear transfer due to the existence of the protective sleeve. The sleeve that had fallen off in Fig.2 was caused by the sleeve breaking and then being pulled out. In practical engineering applications, the armored optical cable is commonly used, where the sleeve has good ductility and high strength and is unlikely to break. On the other hand, for tunnels that are monitored by distributed optical fibers, the length of the embedded optical fibers in the structure can usually be from several hundred meters to several kilometers. The

peak shear strength of the backfill material– sensing cable interface is high, so in general, the optical fibers are unlikely to be pulled out from the structure.

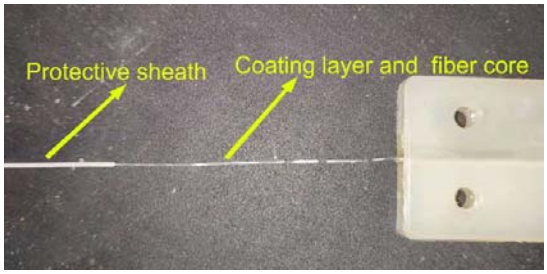

Fig. 2 Photo of the optical fiber protective sleeve shedding

2.2 Theoretical analysis of the strain transfer model

Based on the above analysis, the following strain transfer model could be established, which consists of three layers: (1) the structure to be tested; (2) the protective sleeve; and (3) the optical fiber. The strain transfer between the structure to be tested and the optical fiber is directly realized through the protective sleeve, and there is no sliding between the layers. The schematic diagram of the model is shown in Fig.3.

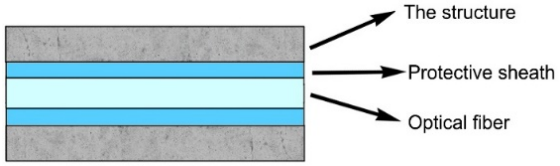

Fig. 3 Structural mechanics model of optical fiber core, protective sleeve and structure

A cylindrical coordinate system is established for the model. x is the axial coordinate of the optical fiber; r is the radial coordinate; and the coordinate origin is the center of the optical fiber layer. The total length of the optical fiber is taken as $2L$. By establishing the equilibrium equation, the relationship between the strain of the optical fiber and the strain of the structure to be measured can be derived.

2.2.1 Stress equilibrium equation establishment

First, only the effect of axial stress and shear stress is considered in the optical fiber, an equilibrium equation of the optical fiber layer is established. Taking the length of the fiber micro-unit is dx, and assuming the shear stress is distributed uniformly; the force of the micro-unit is shown in Fig.4.

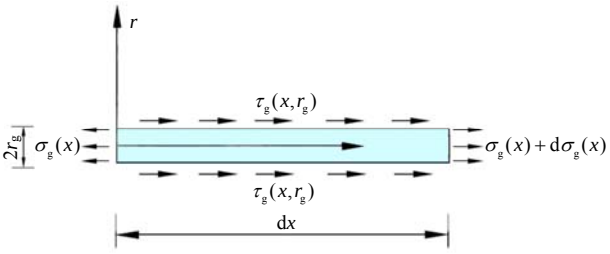

Fig. 4 Force diagram of fiber layer micro-element

The horizontal force balance equation is

$$-\sigma_g(x)\pi r_g^2+[\sigma_g(x)+d\sigma_g(x)]\pi r_g^2+2\pi r_g dx\cdot\tau_g(x,r_g)=0 \quad (1)$$

Eq.(1) can be simplified as

$$\tau_g(x,r_g)=-\frac{r_g}{2}\frac{d\sigma_g(x)}{dx} \quad (2)$$

where $\tau_g(x,r_g)$ is the shear stress along the surface of the optical fiber; $\sigma_g(x)$ is the axial normal stress; and r_g is the radius of the optical fiber layer.

As for the protective sleeve, the shear stress on its inner surface and the shear stress on the surface of the optical fiber are a pair of force and reaction forces, as shown in Fig.5.

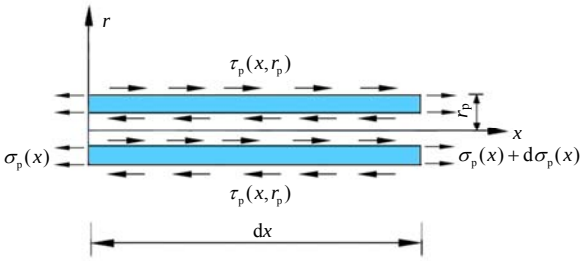

Fig. 5 Force diagram of protective sleeve element

The equilibrium equation is established for the micro-unit:

$$-\sigma_p(x)\pi(r_p^2-r_g^2)+[\sigma_p(x)+d\sigma_p(x)]\pi(r_p^2-r_g^2)-\tau_g(x,r_g)2\pi r_g+\tau_p(x,r_p)2\pi r_p=0 \quad (3)$$

Eq.(3) can be further simplified as

$$\tau_p(x,r_p)=\frac{r_g}{r_p}\tau_g(x,r_g)-\frac{r_p^2-r_g^2}{2r_p}\cdot\frac{d\sigma_p(x)}{dx} \quad (4)$$

where r_p is the vertical distance from the sleeve outer surface to the coordinate axis; $\tau_p(x,r_p)$ is the shear stress of the protective sleeve surface; and $\sigma_p(x)$ is the axial normal stress.

2.2.2 Displacement equilibrium equation establishment

Because of the existence of the protective sleeve, there is a somewhat different between the displacement $u_r(x)$ of the tested structure and the displacement $u_g(x)$ of the optical fiber, which results from the shear strain of the protective sleeve[18], as shown in Fig.6.

The equation of the displacement and the shear strain can be expressed as

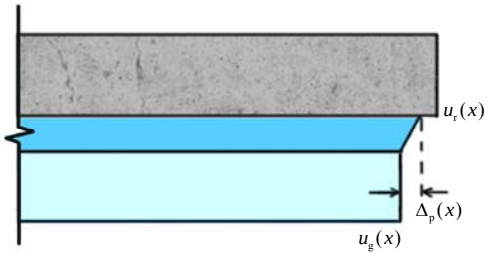

Fig. 6 Schematic diagram of displacement balance relation of optical fiber layer

$$u_{\mathrm{r}}(x)-u_{\mathrm{g}}(x)=\Delta_{\mathrm{p}}(x)=\int_{r_{\mathrm{g}}}^{r_{\mathrm{p}}}\gamma(x,r)\mathrm{d}r \tag{5}$$

where $u_{\mathrm{r}}(x)$ is the displacement of the structure to be tested; $u_{\mathrm{g}}(x)$ is the displacement of the optical fiber layer; and $\gamma(x,r)$ is the shear strain of the protective sleeve. The relation between the shear strain and the shear stress can be denoted as

$$\tau(x,r)=G\gamma(x,r) \tag{6}$$

where G is the shear modulus of the protective sleeve.

2.2.3 Strain differential equation establishment of the optical fiber and the tested structure

The shear stress $\tau(x,r)$ at any point in the protective sleeve [29]:

$$r\tau(x,r)=r_{\mathrm{g}}\tau_{\mathrm{g}}(x,r_{\mathrm{g}}),\ r_{\mathrm{g}}\leqslant r\leqslant r_{\mathrm{p}} \tag{7}$$

By substituting Eq.(2) into Eq.(7), then

$$\tau(x,r)=-\frac{r_{\mathrm{g}}^2}{2r}\frac{\mathrm{d}\sigma_{\mathrm{g}}(x)}{\mathrm{d}x} \tag{8}$$

By replacing the axial normal stress of the optical fiber in Eq.(8) in terms of strain, then

$$\tau(x,r)=-E_{\mathrm{g}}\frac{r_{\mathrm{g}}^2}{2r}\frac{\mathrm{d}\varepsilon_{\mathrm{g}}(x)}{\mathrm{d}x} \tag{9}$$

Where E_{g} denotes the elastic modulus of the optical fiber; and $\varepsilon_{\mathrm{g}}(x)$ represents the axial strain of the optical fiber layer.

By substituting Eq.(9) into Eq.(5), we get:

$$u_{\mathrm{r}}(x)-u_{\mathrm{g}}(x)=-\frac{E_{\mathrm{g}}r_{\mathrm{g}}^2}{2G_{\mathrm{p}}}\frac{\mathrm{d}\varepsilon_{\mathrm{g}}(x)}{\mathrm{d}x}\int_{r_{\mathrm{g}}}^{r_{\mathrm{p}}}\frac{1}{r}\mathrm{d}r \tag{10}$$

Then the following equation can be derived:

$$u_{\mathrm{r}}(x)-u_{\mathrm{g}}(x)=-\frac{E_{\mathrm{g}}r_{\mathrm{g}}^2}{2G_{\mathrm{p}}}\ln\frac{r_{\mathrm{p}}}{r_{\mathrm{g}}}\frac{\mathrm{d}\varepsilon_{\mathrm{g}}(x)}{\mathrm{d}x} \tag{11}$$

Deriving both sides of Eq.(11) with respect to x leads to

$$\frac{\mathrm{d}^2\varepsilon_{\mathrm{g}}(x)}{\mathrm{d}x^2}\frac{E_{\mathrm{g}}r_{\mathrm{g}}^2}{2G_{\mathrm{p}}}\ln\frac{r_{\mathrm{p}}}{r_{\mathrm{g}}}-\varepsilon_{\mathrm{g}}(x)=-\varepsilon_{\mathrm{r}}(x) \tag{12}$$

where $\varepsilon_{\mathrm{r}}(x)$ is the strain of the structure to be tested.

Because a uniform distribution of the strain of each part for the structure is considered, that is to say, the strain is independent of x; in this consideration, $\varepsilon_{\mathrm{r}}(x)$ can be then denoted as ε_{r}.

Assuming

$$k^2=\frac{2G_{\mathrm{p}}}{E_{\mathrm{g}}r_{\mathrm{g}}^2\ln\dfrac{r_{\mathrm{p}}}{r_{\mathrm{g}}}} \tag{13}$$

Eq. (12) can be simplified as

$$\frac{\mathrm{d}^2\varepsilon_{\mathrm{g}}(x)}{\mathrm{d}x^2}-k^2\varepsilon_{\mathrm{g}}(x)=-k^2\varepsilon_{\mathrm{r}} \tag{14}$$

Eq. (14) is the strain differential equation of the structure to be tested and the strain of the optical fiber. Through solving the differential equation, the relation between the optical fiber and the structure can then be obtained.

The general form of the solution for Eq.(14) is

$$\varepsilon_{\mathrm{g}}(x)=A\mathrm{e}^{kx}+B\mathrm{e}^{-kx}+\varepsilon_{\mathrm{r}} \tag{15}$$

where A and B are the integral constants that are determined by the boundary conditions.

Since there is no strain outside the length of the optical fiber layer, the boundary conditions can be defined as follows:

$$\varepsilon_{\mathrm{g}}(L)=\varepsilon_{\mathrm{g}}(-L)=0 \tag{16}$$

By substituting the boundary conditions into the general solution equation, then:

$$A=B=-\frac{\varepsilon_{\mathrm{r}}}{2\cosh(kL)} \tag{17}$$

Then, the axial strain equation of the optical fiber is

$$\varepsilon_{\mathrm{g}}(x)=\varepsilon_{\mathrm{r}}\left[1-\frac{\cosh(kx)}{\cosh(kL)}\right] \tag{18}$$

Equation (18) describes the relationship between the axial strain of the optical fiber and the axial strain of the structure. This relation can be used to determine the strain distribution of the optical fiber after the strain of the tested structure is transmitted through the fiber protective sleeve.

From Eq.(18), the strain transfer rate at each point of the optical fiber embedded in the structure can be expressed as

$$\alpha(x)=\frac{\varepsilon_{\mathrm{g}}(x)}{\varepsilon_{\mathrm{r}}(x)}=1-\frac{\cosh(kx)}{\cosh(kL)} \tag{19}$$

To verify the accuracy of the theoretical result, a finite element analysis of the structure-protective sleeve-optical fiber complex is conducted. The finite element model is shown in Fig.7.

The general physical parameters in Tab.1 are taken as an example to assign the parameters of each domain of the model. 0.5 MPa axial tension stress is applied to both ends of the structure. No force is applied to the protective sleeve and optical fiber. The distribution of the axial strain in the complex is presented in Fig.8.

Figure 8 shows the axial strain distribution of each portion of the model by taking a section from the model central plane. A boundary effect is observed for the strain transmission area of the optical fiber. It is seen that the strain distribution in the central part of the optical fiber is the same as that of the structure, while the strain at both ends of the optical fiber is smaller than that of the structure. This observation results from the shear lag effect. That is, due to the existence of shear stress in the sleeve layer, the longitudinal displacement of the layer is distributed unevenly in the vertical height direction. This phenomenon will cause the attenuation effect of the structure strain when it is transferred to both sides of the optical fiber. Using the deformation magnification function in the finite element software, the deformation of the end could be magnified and displayed, as shown in Fig.9. It can be clearly seen from Fig.9 that, due to the shear

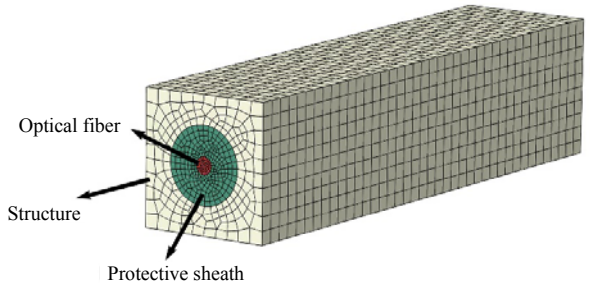

Fig. 7 Finite element model of structure-protective sleeve-optical fiber layer complex

Table 1 Physical properties of optical fiber, protective sleeve and structure

Elastici modulus of optical fiber E_o /GPa	Elastic modulus of protective sleeve E_p / GPa	Elastic modulus of structure E_c /GPa	Poisson's ratio of protective sleeve μ	Outer diameter of protective sleeve r_p /mm	Outer diameter of optical fiber r_o /mm	Optical fiber length L /mm
72	3	30	0.3	1.5	600	40

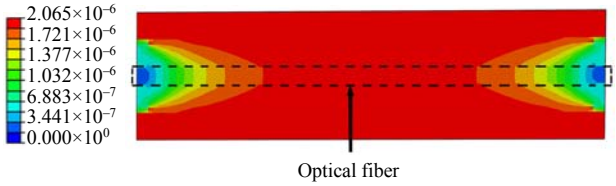

Fig. 8 Axial strain distribution of structure-protective sleeve-optical fiber layer complex

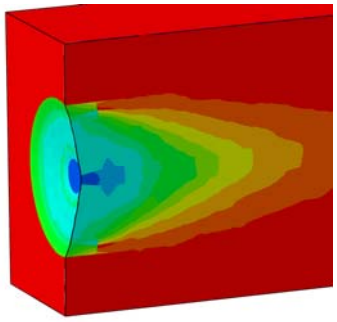

Fig. 9 Schematic diagram of the shear lag effect of structure-protective sleeve-optical fiber layer complex

lag effect, a funnel-shaped non-uniform deformation region is formed at the model end area, and the optical fiber is located in the middle of the funnel-shaped region. This means that at the model end, the deformation of the structure to be measured is not fully transferred to the optical fiber, and the optical fiber remains in the original shape at the model end area and does not stretch as the structure deforms.

To prove the accuracy of the theoretical derivation results, the values from Tab. 1 are applied into Eq.(19), the strain transfer rate of each point in the embedded part of the optical fiber is estimated. The strain transfer rate comparison between the modeling results of the finite element method and the estimation values from Eq. (19) is shown in Fig. 10. It is found that the distribution of the strain transfer rate estimated from the two methods is basically agreed with each other. The strain distribution in the middle part of the two methods is the same, but the strain distribution at both the ends is slightly different, which further prove the accuracy of the theoretical derivation results.

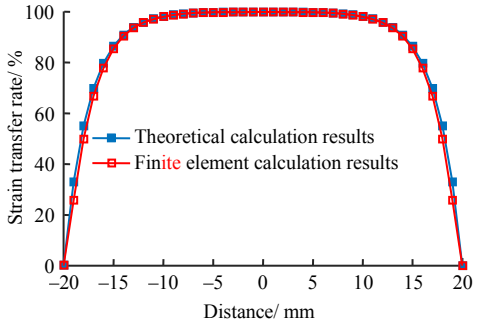

Fig. 10 Fiber strain transmission rate with a 40 mm in length

It is worth to mentioned that there are many assumptions in the above theory and many factors could affect the strain transfer of optical fiber in practical engineering applications. In this consideration, further laboratory experiments are required to explore the coupling effect between the embedded optical fibers and the structure to be measured.

3 Boundary effect test of optical fiber strain transfer in reinforced concrete structure

3.1 Preparation of the reinforced concrete beam specimen

Different types of concrete lining structure are used in tunnel. To simply test the strain transfer effect of an optical fiber in a reinforced concrete lining, reinforced concrete beam specimens were designed and used in the tests. The dimension of the reinforced concrete beam is that, length× width× height(2 000 mm× 120 mm× 200 mm). The concrete strength grade was C_{30}. The secondary steel grade HRB335 with a diameter of 16 mm was selected as the lower loading reinforcing bar. 8 mm diameter steel was selected as the stirrup and the erection reinforcement with a 10 mm diameter. The thickness of the protective layer was 22 mm. Two sets of test specimens were made to eliminate accidental factors and accidents.

3.2 Layout of the optical fiber and the strain gauges

After the reinforced concrete beams were fully cured, at the same height as the steel bar at the bottom, the beam surface was grooved (width× depth: 10 mm× 10 mm) along the direction of beam length. The optical fibers were embedded in the concrete and then sealed with cement mortar, as shown in Fig. 11.

Strain gauges were also attached to the reinforced concrete beam to compare and verify the record data between the stain gauges and the optical fibers. The bottom reinforcement surface was grinded. For purpose of avoiding short-circuit, an insulating paper was pasted on the reinforcing bar and the strain gauge was then pasted onto it. Subsequently, the strain gauges were coated with epoxy resin to protect the strain gauges. The strain gauge No.② was located in the middle of

the bottom longitudinal reinforcement, and No. ① and No. ③ were located 100 mm away from the ends of the longitudinal reinforcement, as shown in Fig. 12.

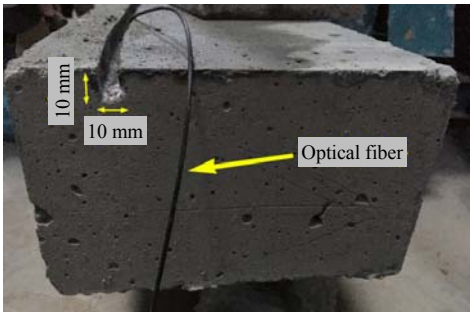

Fig. 11 Embedding of optical fiber in concrete beam

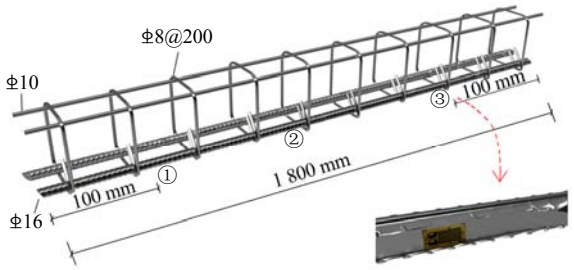

Fig. 12 The location of strain gauge in steel cage (unit: mm)

4 BOFDA monitoring technology and test loading system

4.1 BOFDA distributed optical fiber monitoring technology

In these tests, an FTB2505 Brillouin optical frequency domain optical fiber strain/temperature analyzer, made in Germany and based on BOFDA(The Brillouin Optical Frequency Domain Analysis) technology was used. The test parameters of the instrument were set as follows: 10 ns of pulse width, $\pm 2\times10^{-6}$ of strain measurement accuracy, 1.468 of refractive index, initial frequency, and termination frequency of the instrument 10.5 and 11.0 GHz, respectively. This frequency range can theoretically measure a large strain of 1250×10^{-6} without overflowing the Brillouin frequency shift. The central frequency of the optical fiber is $fB(0)=10.8390$ GHz, and the frequency interval was 5 MHz. To make the data more accurate, 0.05 m of sampling interval of the instrument and 0.2 m of the spatial resolution were used.

4.2 Test strain optical type

A type of new tight sleeve strain sensing fiber (diameter: 2mm, sleeve material: polyurethane) was used and optical type was a new strain optical fiber specially developed for monitoring strain based on an ordinary strain optical fiber. The developed strain sensing fiber not only has good ductility but more importantly, it also solves the problem of relative slippage between the ordinary packaged optical fiber and the sleeve, as shown in Fig. 13.

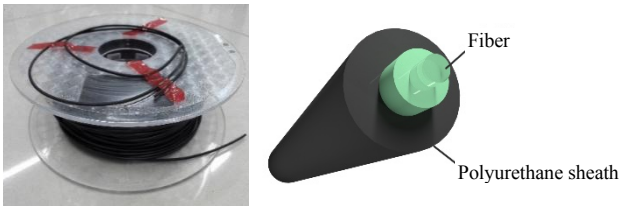

Fig. 13 New tight set strain sensing fiber

4.3 Test loading method

A microcomputer controlled electro-hydraulic servo multi-point coordinated loading fatigue test system was used in the test. The maximum uniaxial loading limit was 500 kN. The displacement loading control was adopted in the test, as shown in Fig.14.

The loading mode of a simply supported beam was used for the beam loading, as shown in Fig. 14 (b). The test beam was firstly pre-loaded 5 minutes, the initial data was recorded for the three strain gauges and the optical fiber. The experiment was divided into two cases. The loading rate was 2 mm/100 s for the first test case. After the initial data was recorded, the strain gauge and optical fiber strain measurements were then conducted, and the next stage was subsequently loaded. The loading rate was 3 mm/100 s for the second test case, the other steps were the same as the first test case.

(a) Laboratory layout

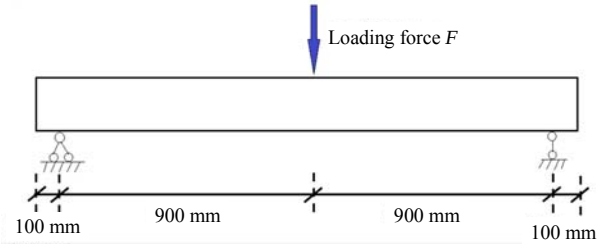

(b) Diagram of beam loading

Fig. 14 Laboratory layout

5 Test results and analysis

Figures 15 and 16 show the test result comparison between the optical fiber and strain gauge for the No. 1 and No.2 test beams under different loading levels, respectively. It is seen that the measured strain data in the middle part of the beam is identical for both the optical fiber and the strain gauge at each loading level, while for the measured test data at both ends of the

beam, it is found that the recorded data from the optical fiber is smaller than those from the strain gauges. This observations mean that the strain in the middle of the beam is accurately measured by the optical fiber, but the strain at both ends of the beam is not fully transmitted to the optical fiber. The test result is in good agreement with the result derived from the theoretical model.

For the No.1 test beams, as shown in Fig.15, when the loading grade is 1, 4, 8, 12mm and 20mm, the average difference value between the recorded data from the optical fiber and the strain gauge is 22×10^{-6}, 67×10^{-6}, 119×10^{-6}, 190×10^{-6}, 422×10^{-6}, and the strain transfer efficiency is 53%, 44%, 51%, 48%, 47%, respectively. Most of the transfer efficiency is around 50%. As the loading grade increases, the deformation of the beam increases, and the difference of the recorded value also increases between the optical fiber and strain gauge on both ends of the beam.

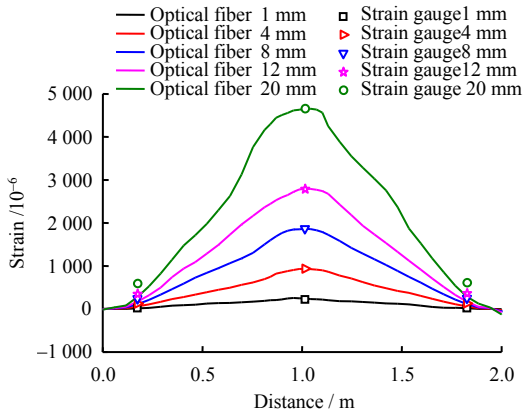

Fig. 15 Comparison of test results of optical fiber and strain gauge for test beam No. 1

In addition, as seen from Fig. 16, the test results of the No. 2 test beam basically follow the same trends when compared with the results of the No. 1 test beam. The deformation in the middle of the beam is fully transferred to the optical fiber. At either end of the beam, the strain transfer efficiency of the optical fiber is 50%, 48%, 52%, 48% for the loading grade of 2, 6, 10, 12, 16 mm, respectively. Based on Eq.(19), the strain transfer efficiency is calculated as 46.8% for the optical fiber at the location. The calculated strain transfer efficiency is consistent with the test results. The observations indicate that the strain transfer efficiency of the optical fiber will not change with the changing of the loading grade.

The above strain transfer tests of the reinforced concrete beams have further verified the accuracy of the theoretical deduction results. The optical fibers that are embedded in the middle of the concrete structure could accurately reflect the deformation of the structure. For the optical fiber at both ends of the beam, the error could be within an acceptable range when the deformation of the concrete structure is not large. In the failure evolution process of the tunnel lining structure, the main deformation is small without significant deformation. Therefore, it can be safely considered that the boundary effect has little influence on the monitoring of the tunnel project. The distributed optical fiber embedded in the tunnel lining structure to monitor the deformation is theoretically feasible.

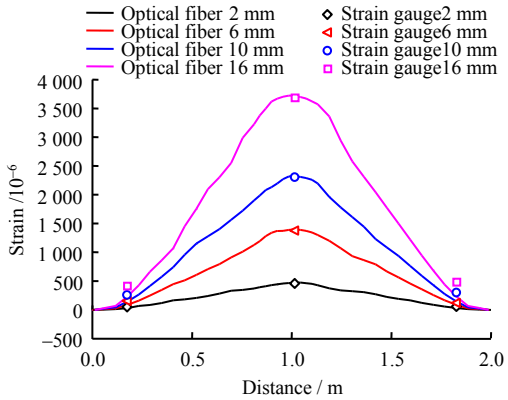

Fig. 16 Comparison of test results of optical fiber and strain gauge for test beam No. 2

6 Engineering application

To explore the influence of the boundary effect on the monitoring effect in the field of engineering, it is necessary to conduct engineering application on the boundary effect of the embedded distributed optical fiber sensor. In this study, an optical fiber was embedded in the concrete lining structure for the optical fiber monitoring project of the metro section of the Beijing New Airport Line, and the monitoring effect was then analyzed.

6.1 Overview of the engineering project

The work area 2 of the civil engineering 07 project was the main work area for the first phase project of the new airport line of the Beijing Rail Transit. The construction task was in the range from the air shaft section #2 to the air shaft section #1. The construction mileage was from K33+208.249 m to K35+545.227 m, which included an underground excavation sector (90.995m), a shield well and cut-and-cover sector (130.9 m), and a double line shield sector (2119.7 m).

The underground excavation section started with K35+454.232 m and ended at K35+544.232 m. The total length of the double line was 90.995 m with a slope of 20‰. The cross-section of the excavation was a single-hole horseshoe-shaped section with 10.7–12.0 m of soil cover. The CRD(cross diaphragm) method was used for the excavation and the construction of the initial lining. The secondary lining was constructed with a reinforced concrete structure. The dimension of the underground tunnel was 8.9 m in width and 9.09 m in height. The thickness of the initial lining structure was 300 mm, with 30 mm thick protective layer. This monitoring project was mainly conducted in the right line of the underground excavation section.

According to the on-site construction schedule, the left and right lines of the underground excavation were

divided into 15 construction sections, each section was 6 m in length, as shown in Fig.17. The first construction section corresponds to 90 m of the abscissa in the following analysis curve, and the fifteenth construction section corresponds to 0 m of the abscissa in the following analysis curve. The construction of the secondary lining adopted the sequence construction method. The bottom shoring was dismantled in sections and concrete was then poured in an inverted arch. After the concrete was poured in the inverted arch, the upper and cross shoring was dismantled in sections and the concrete of the secondary lining side wall and the vault was poured. There were convergence and vault settlement measurement points on both sides of the tunnel and the middle line of the vault, respectively, which were used to monitor the convergence and settlement deformation of the tunnel. The vault settlement was measured using a high precision total-station. The convergence of the side walls was measured using a steel ruler convergence meter with anchor piles and hooks which were embedded in the tunnel side wall. The interval of each monitoring section was 15 m.

Fig. 17 Schematic diagram of the division of the second lining construction section

6.2 Optical fiber layout

The optical fiber layout method was the buried layout type, as illustrated in Section 3.2. To facilitate the comparison with the monitoring data of the construction team, the location of the optical fibers was located at the observation points of the tunnel side walls' clearance convergence and vault settlement (see Fig. 18). After the initial lining support construction of the tunnel, grooves were cut into the initial concrete lining surface along the entire tunnel length (see Fig. 19). The depth of the grooves was 1 cm. The optical fibers were put into the grooves and sealed with quick-setting high-strength mortar. The fibers that were buried in the side walls of No. 1 and No. 3 pilot tunnels were marked as No. 1 and No. 3 fibers, and the fiber that was buried in the vault was marked as No. 2 fiber.

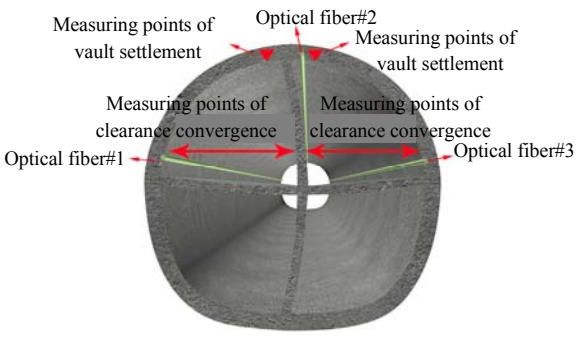

Fig. 18 Locations of the placement of optical fibers

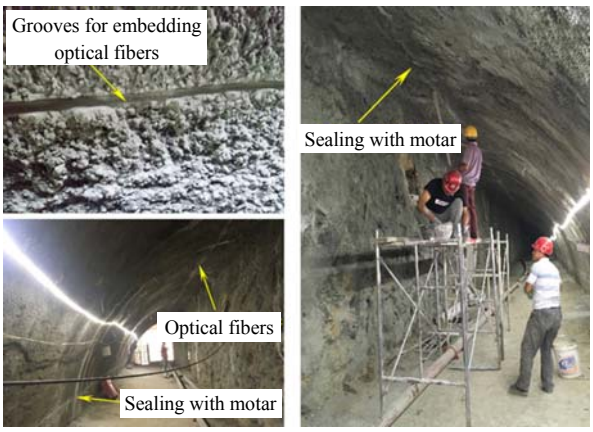

Fig. 19 Placement process of the optical fibers

6.3 Analysis of the monitoring results

Due to the poor strain transfer efficiency of the optical fiber at the end of the structure, the first–fifth sections of the tunnel end were selected to analyze the monitoring results during the process of removing the temporary shoring and constructing the secondary lining. During the process of removing the temporary support, the stress transformation of the tunnel structure was complicated. To better analyze the deformation rule of the tunnel during the process, a finite element model was established according to the field stratum distribution, as shown in Fig. 20.

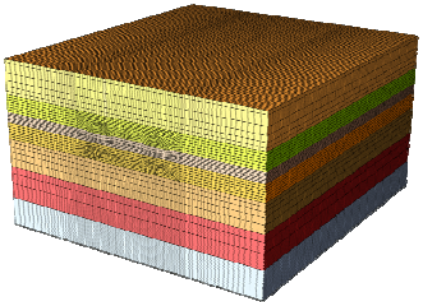

Fig. 20 The finite-element modeling model

Boundary constraints were applied according to the formation conditions in the field, and the top surface was set as a free boundary. Displacement constraints were applied on the front, back, left, right, and lower boundaries of the model. The method of killing element was used to simulate the excavation of the tunnel and the dismantling of the temporary shoring in the tunnel, and the method of activating elements was used to model the construction of the primary lining and the secondary lining of the tunnel.

As the construction was divided into many sections of the second lining from the first to fifth sections and due to the length limitation of this paper, six representative working conditions were selected for analysis. Working condition 1 was simulated as the dismantling process of the first, third, and fifth bottom shoring (under all working conditions, the temporary shoring was dismantled at the same time). Working condition 2 was simulated as the pouring process of the concrete of the first, third

and fifth sections of the inverted arch, and then the dismantling process of the bottom shoring of the second and fourth sections of the inverted arch. Working condition 3 was simulated as the pouring process of the concrete of the second and fourth sections of the inverted arch, and then the dismantling process of the first, third, and fifth sections of the cross shoring. Working condition 4 was simulated as the dismantling process of the first, third, and fifth sections of the upper shoring. Working condition 5 was simulated as the pouring process of the concrete of the first, third, and fifth sections of the secondary lining of the side walls and the vault, and then the dismantling process of the second and fourth sections of the cross shoring. Working condition 6 was simulated as the demolishing process of the middle wall of the second and fourth sections of the upper shoring. The remaining working conditions were simulated as a repetition of several cycles of the above working conditions until the construction of the secondary lining was completed. The schematic diagram of each working condition is shown in Fig.21.

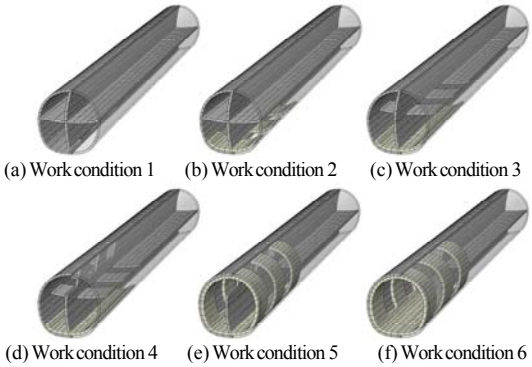

Fig. 21 Schematic diagram of modeling cases 1–6

Referring to the actual buried location of the No. 2 optical fiber, an identical path was selected in the same location of the tunnel's FEM model, and the results of the settlement of the above nodes were compared with the measured strain values from the optical fibers.

Figure 22 shows the comparison of the vault's settlement curve from the modeling and the optical fiber's strain curve. It is seen from the Fig.22 that for working conditions 1 to 6, the removal of the second and fourth sections of the bottom shoring (working condition 2) has the greatest impact on the vault settlement. The reason is the bottom of the vault is in a suspended state from the first to the fifth tunnel sections and there is no ground support at these sections, which results in a large settlement deformation of the tunnel. The root of the cantilever end near the vault of the sixth section was subjected to the largest bending moment and also generated the largest tensile strain of the optical fiber.

Referring to the actual buried location of the optical fibers No. 1 and No. 3, similar paths were selected in the same location of the FEM model of the tunnel. The lateral deformation modeling results of each node along the paths were then compared with the field measured strain from the optical fibers and the result is shown in Fig.23. When the temporary support is removed, it is seen that the strain of the optical fibers No. 1 and No. 3 is around 0, which indicates that there is no deformation occurred in the side wall embedded fibers. According to the numerical simulation curve of the deformation at the tunnel side walls, the lateral deformation of the side wall varies within a very small range, and the maximum convergence value of the measured data from the field is smaller than 2 mm after the supports are dismantled. This observation is because the lateral soil pressure is smaller than the vertical soil pressure. The settlement of the vault leads to the two tunnel sides expanding outwards, which also provides a part of the lateral resistance. The result indicates that dismantling the temporary shoring has a negligible effect on the lateral deformation of the tunnel's sidewall. The strain curves from the optical fiber are in good agreement with the field monitoring results, which further indicates the feasiblility to use distributed optical fibers to monitor the lateral deformation of a tunnel's sidewall.

From the above analysis, it is seen that dismantling the temporary shoring has a significant impact on the vault settlement. It is therefore necessary to focus the research on monitoring the vault settlement. As the optical fibers are buried in the axial direction of the tunnel, those optical fibers can only monitor the horizontal deformation of the tunnel and the measured data are the strain of the optical fibers, which cannot directly reflect the vertical vault settlement. To solve this issue, it is necessary to study the calculating method of the vault's settlement from the inversion strain of the optical fiber.

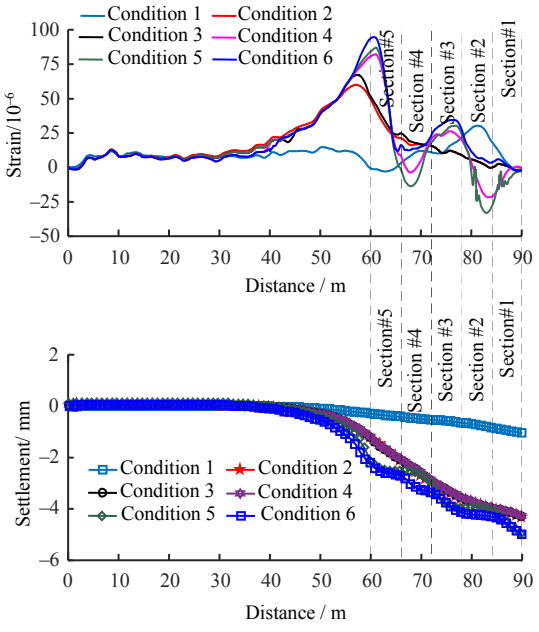

Fig. 22 Strain value of the No.2 optical fiber and numerical simulation value of the vault settlement

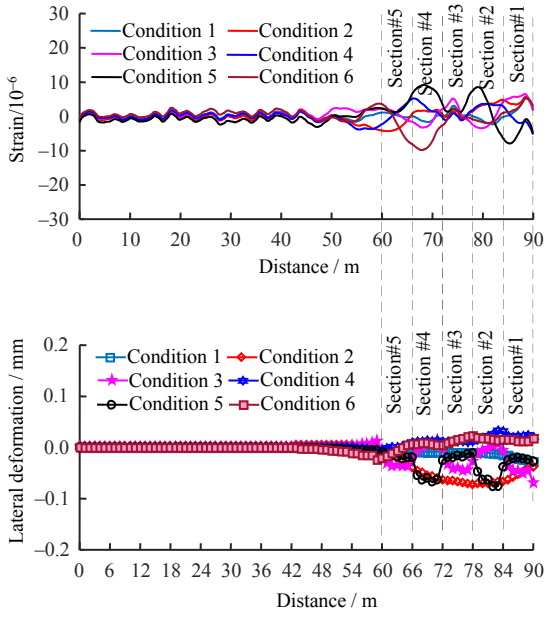

(a) Comparison of strain of optical fiber No.1 and numerical simulation value of side wall lateral deformation

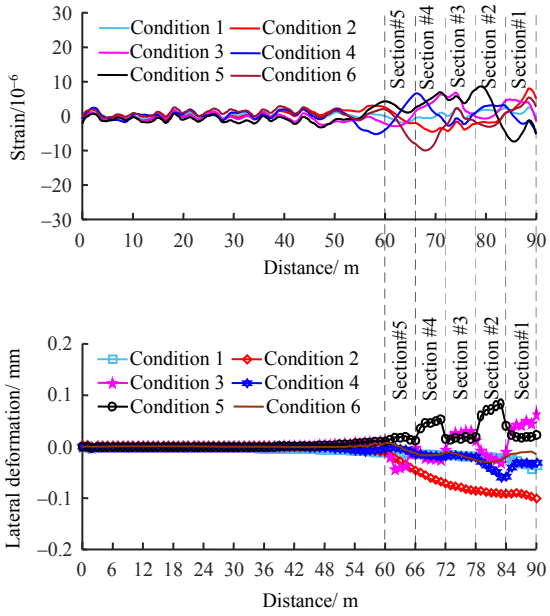

(b) Comparison of strain of optical fiber No.3 and numerical simulation value of side wall lateral deformation

Fig. 23 Strain values of optical fibers and simulated horizontal deformation value of side wall

Through the analysis of the vault settlement curve from the numerical simulation, it is found that the vault settlement model is very close to a quadratic function when the temporary shoring is removed. Figure 24 shows the effect of fitting the vault settlement curves with a quadratic polynomial for the different working conditions, and the R^2 values are above 0.97. Therefore, the vault settlement law conforms to the form of a quadratic curve $y = ax^2 + bx + c$ when the temporary shoring is removed. As the tunnel structure at the point 0 m is far away from the construction area at the tunnel working face, where the supports were being dismantled, this tunnel area is unaffected by the dismantling process. Therefore, this point could be considered as a reference point and its vault settlement value is assumed to be 0. That is: when $x = 0$, the settlement $y = 0$. Then the vault's settlement curve can be simplified to the form of $y = ax^2$. Based on the discussion, an inversion model of the vault settlement is established based on the strain in the optical fiber, as shown in Fig. 24.

Assuming the tunnel length is in the range of $(0, L)$, then when the vault subsides, the optical fiber embedded in the vault will generate a certain length increment ΔL, which will be the arc length s of the deformed optical fiber in the range $(0, L)$ minus the original length L of the optical fiber, as shown in Fig. 24.

The incremental length of the fiber is

$$s - L = \Delta L \tag{20}$$

The elongated length of the optical fiber can be determined using the following equation:

$$L + \Delta L = \sum_{i=0}^{L} \Delta x \varepsilon_i \tag{21}$$

where Δx represents the sampling interval of the optical fiber and ε_i represents the strain of the optical fiber at each sampling point.

The value of s can be calculated using the arc length equation:

$$s = \int_0^L \sqrt{1 + (y')^2}\,\mathrm{d}x \tag{22}$$

where $y = ax^2$

From Eq.(20) to Eq.(22), the expression with the parameter a can be written as

$$\frac{\sqrt{L^2 + 4a^2L^4}}{2} + \frac{a}{8}\ln\frac{\sqrt{1 + 4a^2L^2} + 2aL}{\sqrt{1 + 4a^2L^2} - 2aL} = \sum_{0}^{L} \Delta x \varepsilon_i \tag{23}$$

By solving Eq.(23), the expression of the vault settlement curve can be obtained. The vault settlement can be then inversely calculated based on the strain of the optical fiber under each working condition.

Figure 26 shows a vault settlement comparison between the optical fiber inversion and the field measured data of the total station. For working conditions 5 and 6, to pour the concrete of the secondary lining, the settlement and convergence observation marks at 60 m and subsequent marks were removed prior to the construction. Therefore, only the settlement data for the sections at 0–45 m were obtained. It is seen that the inversion results are basically consistent with the results from the field observation, but there is some deviation in the values. The inversion values from the fiber monitoring data are larger than that of the total station's observation values, and the largest deviation is 2.84 mm. The reasons for this difference are as follows: (1) There are differences between the numerical simulation results and the actual filed monitoring situation. The field situation is more complicated than the model, and therefore the results from the parabolic model cannot fully conform to the actual settlement model of the vault, which could result in the differences between the calculated settlement value from the inversion and the filed observed

settlement value. (2) As the observation frequency of the total station is only once per 24 hours, the errors in the observation would have continuously accumulated, which means that the errors in the accumulated settlement became larger and larger. (3) To facilitate the solution, the vault's settlement curve is simplified into the form of $y=ax^2$. The symmetrical axis of the curve is assumed to be $x=0$, and the influence of the first-order coefficient b on the position of the curve is not considered. This will lead to overall large values after the section at 10 m. This is the main reason that results in the deviation in the results.

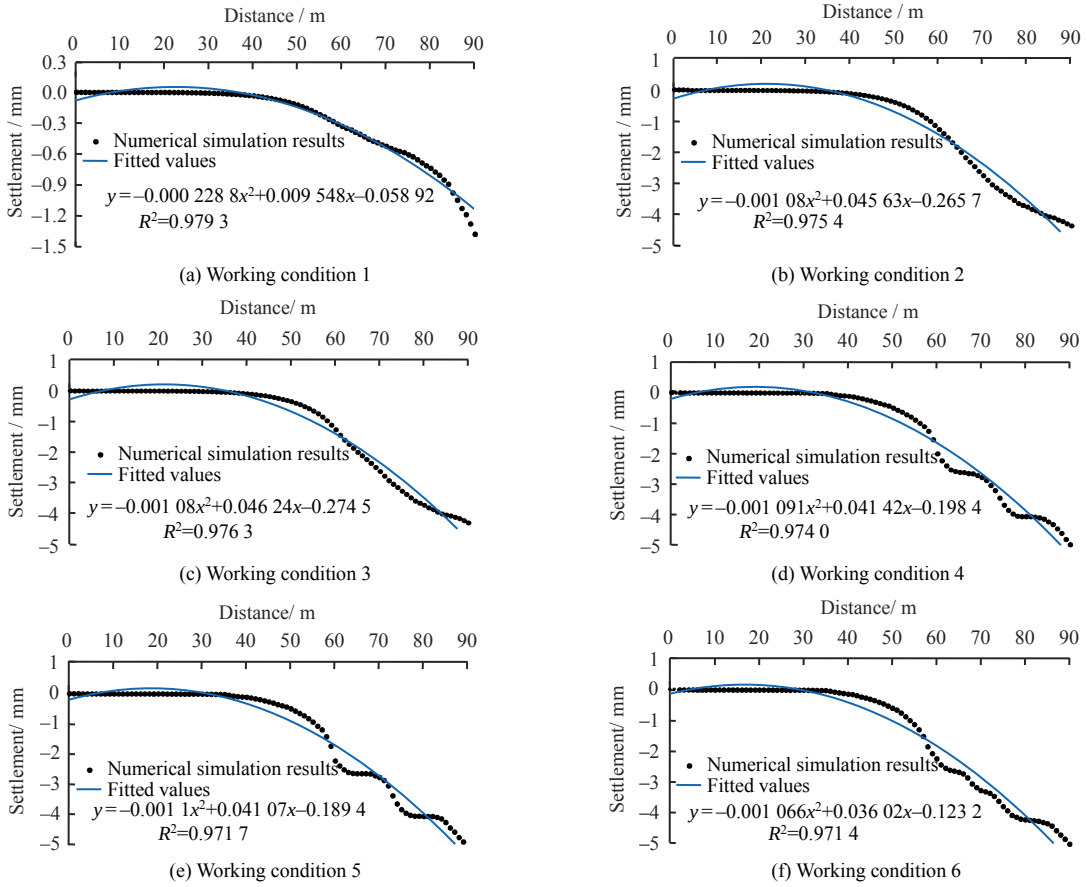

Fig. 24 Numerical modeling curves and quadratic function fitting curves of vault settlement

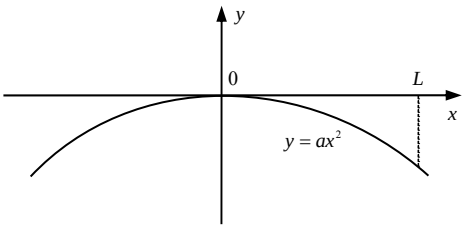

Fig. 25 Calculation model of vault settlement

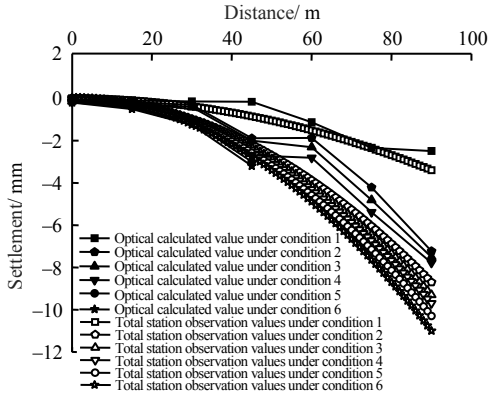

Fig. 26 Comparisons of the optical fiber inversion values and total station observation values of vault settlement

If the curve shape can keep unchanged and its symmetry axis is changed to $x=10$, then the inversion value from the optical fiber is able to correspond well with the observed value of the total station, as shown in Fig. 27. Therefore, if the conditions permit, the settlement monitoring value can be obtained at a certain point using a traditional monitoring method and this value can be then considered as the boundary condition, the first-order coefficient b can also be solved. Once the coefficient b is determined, it can be substituted into the calculation model to improve the accuracy of the inversion calculation of the optical fiber.

From the above engineering application analysis, it is seen that a good agreement is found between the optical fiber curve and the theoretical analysis curve. The tunnel settlement deformation curve derived from the inversion of the optical fiber strain curve can also match well with the field monitoring values, which indicates that a good coupling performance is realized between the embedded optical fiber within the tunnel lining structure and the structure to be tested. The boundary effect has little influence on the monitoring results and the optical fiber can basically fully transmit

the deformation of the monitored structure. It is feasible to apply distributed optical fiber embedded technology to tunnel structural health monitoring.

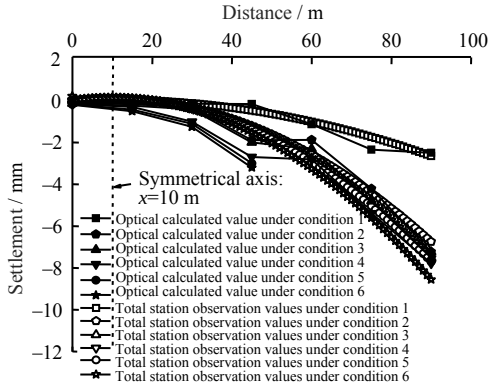

Fig. 27 Comparisons of the modified optical fiber inversion values and total station observation values of vault settlement

7 Conclusion

This study systematically studies the cooperative performance between the embedded optical fiber sensor and the tunnel lining and the boundary effect of the strain transmission behavior from three aspects in terms of theoretical analysis, laboratory experiment, and filed application. The main conclusions are as follows:

(1) The distributed optical fiber is embedded into the tunnel lining as a composite model of a three-layer structure, which consists of structure to be measured-protective sleeve-optical fiber. Based on the three-layer composite model, it is found that the strain transmission of the optical fiber has a boundary effect. A relatively small strain transmission rate is found at both ends area, while for the most area of the central portion, the strain transmission rate is close to 100%. As the buried length of the optical fiber increases, the strain transmission rate increases.

(2) The test results show that the greater the structure deformation, the greater the difference between the strain values measured by the optical fibers on both the sidewalls and the actual values. As for the tunnel deformation with small deformation, even if the strain at the tunnel ends cannot be fully transmitted to the optical fiber, because the absolute value of the error is also very small, the monitoring error caused by the boundary effect is relatively stable for most of the structures and the monitoring error can be safely ignored for tunnel monitoring projects without high test accuracy requirement.

(3) Field engineering application research shows that a good coupling effect is found between the distributed optical fiber and the tunnel lining structure, which verifies the feasibility of embedded distributed optical fiber into the tunnel lining to monitor tunnel deformation. When using the distributed optical fibers for monitoring, the influence of boundary effect should be avoided as much as possible and the monitoring area should be located within the high-efficiency strain transmission area of the optical fiber to ensure the monitoring results more accurate.

References

[1] OHNO H, NARUSE H, KIHARA M, et al. Industrial applications of the BOTDR optical fiber strain sensor[J]. Optical Fiber Technology, 2001, 24(7): 45–64.

[2] HOU Gong-Yu, XIE Bing-bing, JIANG Yu-sheng, et al. Research for the optical fiber strain and the settlement of roof based on BOTDR technology[J]. Rock and Soil Mechanics, 2017, 38(5): 1298–1304.

[3] BERNINI R, MINARDO A, ZENI L. Dynamic strain measurement in optical fibers by stimulated Brillouin scattering[J]. Optics Letters, 2009, 34(17): 2613–2615.

[4] KLAR A, DROMY I, LINKER R. Monitoring tunneling induced ground displacements using distributed fiber-optic sensing[J]. Tunnelling and Underground Space Technology, 2014, 40:141–150.

[5] METJE N, CHAPMAN D, ROGERS C, et al. An optical fibre sensor system for remote displacement monitoring of structures-prototype tests in the laboratory[J]. Structural Health Monitoring, 2008, 7(1): 51–63.

[6] SHI Bin, XU Xue-jun, WANG Di, et al. Study on BOTDR-based distributed optical fiber strain measurement for tunnel health diagnosis[J]. Chinese Journal of Rock Mechanics and Engineering, 2005, 24(15): 2622–2627.

[7] HOU Gong-yu, XIE Bing-bing, JIANG Yu-sheng, et al. Sawtooth layout technology and principle of fiber used in deformation monitoring of roadway subsidence[J]. Rock and Soil Mechanics, 2017, 38(Suppl.1): 96–102.

[8] LI Hong, ZHU Lian-qing, DONG Ming-li, et al. Analysis on strain transfer of surface-bonding FBG on Al 7075-T6 alloy host[J]. Optik, 2016, 127(3): 1233–1236.

[9] SHEN Wei, WANG Xiao-xing, XU Lin, et al. Strain transferring mechanism analysis of the substrate-bonded FBG sensor[J]. Optik, 2018, 154: 441–452.

[10] TORRES BENJAMIN, PAYÁ-ZAFORTEZA IGNACIO, CALDERON PEDRO A, et al. Analysis of the strain transfer in a new FBG sensor for structural health monitoring[J]. Engineering Structures, 2011, 33(2): 539–548.

[11] WANG Hua-ping, JIANG Li-zhong, XIANG Ping. Improving the durability of the optical fiber sensor based on strain transfer analysis[J]. Optical Fiber Technology, 2018, 42: 97–104.

[12] WU Ru-jun, ZHENG Bai-lin, LIU Zhi-gang, et al. Analysis on strain transfer of a pasted FBG strain sensor[J]. Optik, 2014, 125(17): 4924–4928.

[13] LI Bo, ZHANG Dan, CHEN Xiao-xue, et al. Testing method on performance of deformation coupling between distributed sensing fiber and soil[J]. Geological Journal of China Universities, 2017, 23(4): 633–639.

[14] YANG Hao, ZHANG Dan, SHI Bin, et al. Experiments on coupling materials' proportioning of borehole grouting in directly implanted optic fiber sensing[J]. Journal of Disaster Prevention and Mitigation Engineering, 2012, 32(6): 714–719.

[15] CHENG Gang, SHI Bin, ZHU Hong-hu, et al. Experimental study on coupling performance of fiber and sand interface based on distributed sensing[J]. Journal of Disaster Prevention and Mitigation Engineering, 2019, 25(4): 487–494.

[16] SHI Bin, GU Kai, WEI Guang-qing, et al. Full section monitoring of land subsidence borehole using distributed fiber optic sensing techniques[J]. Journal of Engi- neering Geology, 2018, 26(2): 356–364.

[17] ZHANG Cheng-cheng, SHI Bin, ZHU Hong-hu, et al. Theoretical analysis of mechanical coupling between soil and fiber optic strain sensing cable for distributed monitoring of ground settlement[J]. Chinese Journal of Geotechnical Engineering, 2019, 41(9): 1670–1678.

[18] ZHOU Zhi, LI Ji-long, OU Jin-ping. Interface strain transfer mechanism and error modification of embedded FBG strain sensors[J]. Journal of Harbin Institute of Technology, 2006, 38(1): 49–55.

[19] WU You-ming, LUO Qi-zhi, YUE Zhu-feng. Energy-variational method of the shear lag effect in thin walled box girder[J]. Engineering Mechanics, 2003, 20(4): 161–165.